A Microcontroller-Based Power Management System for Standalone Microgrids With Hybrid Power Supply

Bruno Belvedere, Michele Bianchi, Alberto Borghetti, *Senior Member, IEEE*, Carlo Alberto Nucci, *Fellow, IEEE*, Mario Paolone, *Senior Member, IEEE*, and Antonio Peretto

***Abstract*—The paper presents a microcontroller-based power management system (PMS) designed for the online operation of an experimental low voltage microgrid equipped with a battery storage system and two power supplies: a kilowatt (kW)-class proton exchange membrane (PEM) fuel cell (FC) and a photovoltaic (PV) module emulator, both connected to a low voltage ac node. The connections of the energy sources to the common ac bus make use of power inverters with specific functionalities. The ac node feeds electric active and reactive load emulators able to reproduce programmable profiles. The automatic PMS provides the microgrid monitoring and the FC power scheduling in both grid-connected and islanded operating conditions. The paper describes the structure and functionalities of the PMS as well as a specific experimental investigation aimed at assessing the dynamic performance of the microgrid in islanded conditions.**

***Index Terms*—Battery, digital microcontroller, electrical microgrids, fuel cell (FC), photovoltaic (PV) emulator, power management system (PMS).**

I. Introduction

DISTRIBUTED generation (DG) may result in enhanced continuity of service and in increased customer participation to the electricity market [1], [2]. These opportunities are certainly supported by allowing the operation of a small portion of distribution networks (both on medium and low voltage levels) in islanded conditions. The literature on the subject defines microgrids as small-scale power systems equipped with embedded generators and suitable control systems able to supply local electrical and thermal demands in islanded operation. In this definition, microgrids are also designed to connect seamlessly to the public distribution network and, after that, disconnect when appropriate [3]–[7].

In household applications, the above-mentioned capability to operate in islanded mode is permitted by the presence of energy storage devices and by the implementation of automatic scheduling systems that make use of communication and aggregation features allowing the operation and control of microgrids as single entities.

Within this context, there is a general interest for the utilization of kilowatt (kW)-class fuel cells (FCs) in residential applications (e.g., [8]–[10]). Indeed, compared with other conventional small generators, FCs, and in particular the proton exchange membrane (PEM) ones, promise higher cogenerative performance, clean and silent operation, and cost-effective supply of power. Recently, Erdinc and Uzunoglu [11] provided a review of different architectures of systems powered by PEM FCs, also in combined use with other power supply and energy storage units, in order to build so-called hybrid systems.

Various energy management approaches have been proposed in the literature in order to handle the characteristics of different power generators and storage systems. With reference to integrated PEM FC and battery systems for electric vehicle applications, Thounthong *et al.* [12] propose a cascade control of FC-current, battery-current, and battery state-of-charge with a limitation function of the dc-link voltage. Concerning residential applications, hybrid energy storage systems composed by regenerative FCs integrated with batteries, or ultracapacitors, have been compared in order to assess the criteria for the exploitation of the different energy and power density values of the components (e.g., [13], [14]).

Additional research efforts appear to be needed in order to develop automatic systems suitable for residential applications able to take into account the specific technical characteristics, and constraints, of the above-mentioned sources, namely, integration of different electrical and thermal generation systems, reduced-size storage resources, and continuity of supply.

For this purpose, an experimental microgrid has been developed at the authors' laboratory [15], [16]. As shown in Fig. 1, the microgrid includes a PEM FC able to provide 4.5-kW electrical and 4.7-kW thermal outputs (fed by a gaseous hydrogen storage subsystem), a 0.6-kW photovoltaic (PV) emulator, and a 4.2-kW–100-Ah lead-acid battery storage system. All these devices are connected to a common 230-V ac bus through inverters with specific characteristics.[1] The inverter of the PEM FC allows setting its power production taking into account the FC limitations and requirements. One of the PV emulators tracks its maximum power operating point, while the 4.2-kW bidirectional converter of the storage system implements a voltage-frequency control of the ac bus when the microgrid is disconnected

Manuscript received June 27, 2011; revised November 14, 2011; accepted February 04, 2012. Date of publication May 04, 2012; date of current version June 15, 2012. This work was supported in part by the Ministero dell'Università e della Ricerca under Project PRIN 2007 and in part by Regione Emilia Romagna-Provincia di Ravenna under Program Tecnopoli POR FESR 2007-2013.

B. Belvedere was with the Faculty of Engineering, University of Bologna, 40136 Bologna, Italy. He is now with the BMW Research and Innovation Center, 80788 Munich, Germany.

M. Bianchi, A. Borghetti, C. A. Nucci, and A. Peretto are with the Faculty of Engineering, University of Bologna, 40136 Bologna, Italy (e-mail: michele.bianchi@unibo.it; alberto.borghetti@unibo.it; carloalberto.nucci@unibo.it; antonio.peretto@unibo.it).

M. Paolone is with the Distributed Electrical Systems Laboratory, École Polytechnique Fédérale de Lausanne (EPFL), 1015 Lausanne, Switzerland (e-mail: mario.paolone@epfl.ch).

Digital Object Identifier 10.1109/TSTE.2012.2188654

[1] In the literature, different schemes are also proposed and analyzed in which the various components of the hybrid power supply are connected to a common dc bus (e.g., [17]–[19]).

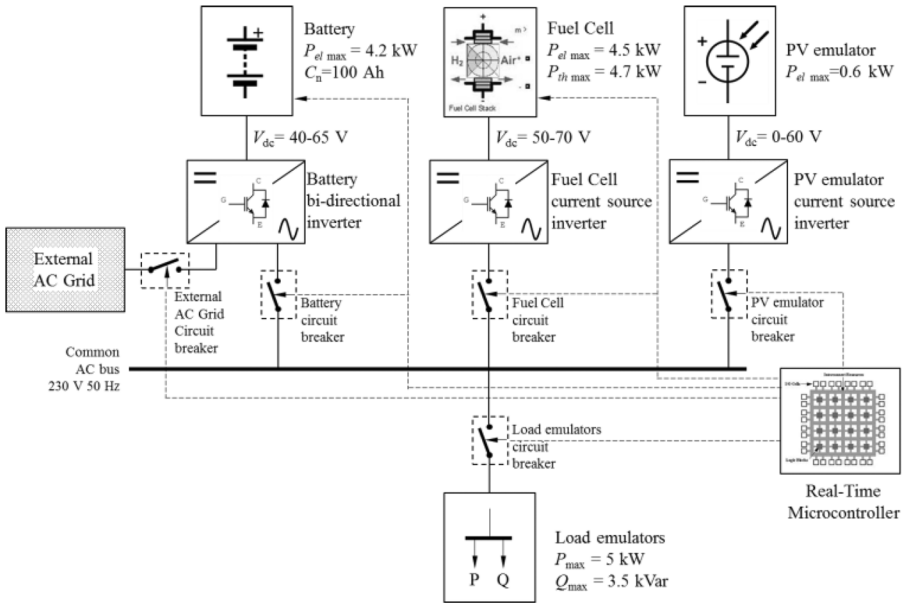

Fig. 1. Architecture of the experimental micro grid.

from the external network [20]. The ac bus feeds electric active and reactive loads, which reproduce programmable profiles through separate on-load tap-changer transformers.

A power management system (PMS) has been developed and implemented into an embedded microcontroller for the automatic operation of the experimental microgrid in standalone conditions. The PMS has been conceived to estimate and control the battery state-of-charge (SOC) as this quantity represents one of the most critical operation elements for the microgrid continuity of supply in islanded operating conditions.

The paper aims at describing the above-mentioned PMS with particular focus on its implementation into a dedicated real-time microcontroller equipped with a field-programmable gate array (FPGA). Moreover, it presents the results of the experimental investigation aimed at assessing the dynamic characteristics of the standalone microgrid under various initial SOC values, electric load profiles, and load rejection maneuver.

The structure of the paper is the following: Section II provides some details on the characteristics of the PEM FC system. Section III describes the PMS functionalities developed to control the FC output with reference to standalone operating conditions of the microgrid. Section IV presents the experimental results obtained during the PMS actions for different load profiles. Section V presents the results of the PMS and microgrid transient response following a sudden and complete disconnection of the electric load (load rejection). Section VI concludes the paper with final remarks.

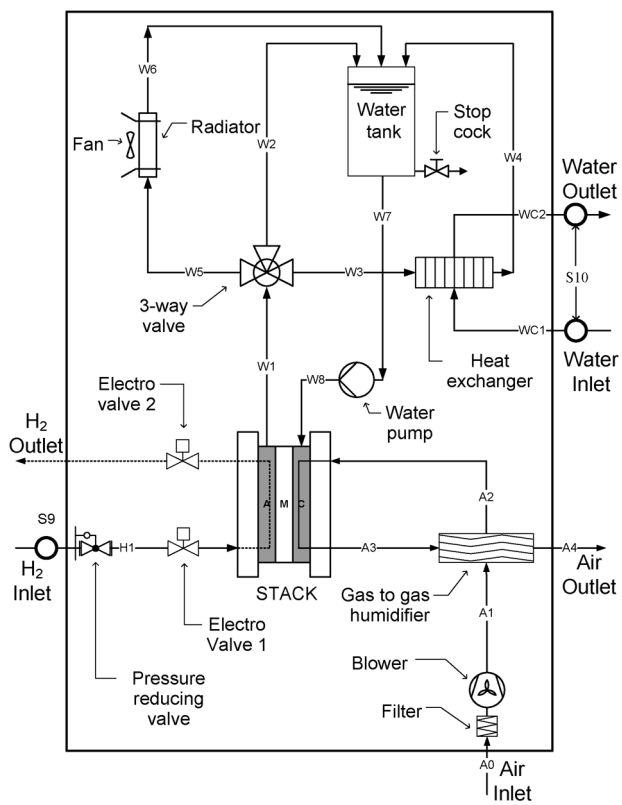

Fig. 2. PEM FC general layout.

II. Description of the PEM FC

Fig. 2 shows the layout of the PEM FC with its hydrogen, air, and cooling water circuits. The FC stack is fed by hydrogen at the anode, coming from an external upstream storage system. The fuel inlet pressure, equal to approximately 3 bar, is reduced to the required 1.8-bar value by means of a pressure-reducing valve. Two electro-valves are placed at the inlet and outlet of the hydrogen line: electro-valve 1 is a safety valve, open in normal conditions; the outlet dead-end valve (electro-valve 2) operates with on–off logic for the water vapor release from the anode.

The air mass flow required by the FC for the electrochemical oxidation reactions is admitted at the cathode side through a blower with variable rotational speed in order to increase the external air pressure up to 1.2 bar.

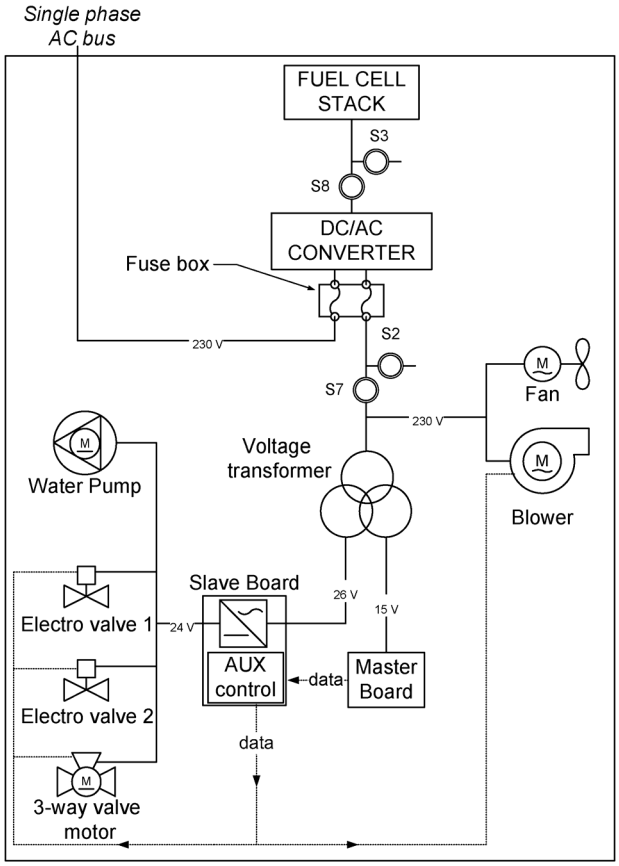

Fig. 3. Electric scheme of the PEM FC with its auxiliaries.

In order to keep the adequate water content in the stack membrane, a gas-to-gas porous-medium humidifier is used. It humidifies the inlet air stream by using the water vapor produced by the hydrogen oxidation and released at the stack cathode. The humidification process requires neither electric energy nor heat from external sources.

The cooling subsystem, also shown in Fig. 2, is aimed at removing the reaction heat by demineralized water fed by means of a pump into the stack. It allows keeping the internal temperature within the range between 60 °C and 70 °C. A three-way valve is positioned at the outlet (W1 in Fig. 2) and it is used to control the water temperature, depending on the system operating conditions, by regulating the water flow to the heat exchanger to the radiator (stream w3 and w5). When the operating conditions require a fast increase of the stack temperature (e.g., during the initial warm-up mode), all the cooling water is bypassed into the tank (stream w2).

Fig. 3 shows the electric scheme of the FC with internal auxiliaries and connection to the external single-phase 230-V ac bus. The FC dc voltage output, characterized by the nonlinear voltage–current relation given by the stack polarization curve [10], varies between 50 and 70 V and it is converted to 230-V ac by an inverter.

As provided by the manufacturer, the inverter of the FC is designed and controlled to operate only in grid-connected mode. For the specific application in the experimental microgrid, its standard anti-islanding protection, based on a continuous evaluation of the network impedance, has been disabled and the allowed frequency-deviation range increased to ± 1.25 Hz (being the rated value of the network frequency equal to 50 Hz).

Some of the electrical auxiliaries, namely the air blower and the cooling fan, are connected to an internal 230-V ac bus. The other auxiliaries are supplied by dc buses at various voltage levels through the ac bus by means of a rectifier unit (slave board in Fig. 3) connected to the secondary winding of a transformer.

The FC auxiliaries characterized by the largest electric power consumption are: the air blower (530 W), the cooling fan (35 W), and the cooling water pump (25 W). The system efficiency is affected also by the losses of the main inverter and of the rectifier of the auxiliaries.

III. Functions of the Automatic PMS

The functions of the automatic PMS have been developed taking into account the following peculiarities of the experimental microgrid, namely: 1) the maximum power provided by the PV array is lower than the maximum power input absorbed by the battery during the charging phase; 2) the FC is requested to operate only when the system is disconnected from the external distribution system.

The PMS control has been developed with a state-chart structure and the relevant main operating modes are:

1) Grid connected operating mode.
   - 1.1) $\mathrm{SOC} < \mathrm{SOC}_{\max}$;
   - 1.2) $\mathrm{SOC} = \mathrm{SOC}_{\max}$.
2) Islanded operating mode.
   - 2.1) FC in operation.
     - 2.1.1) $P_{\mathrm{load,PV}} < P_{\mathrm{FC,max}} + P_{\mathrm{batt,max}}$ and $\mathrm{SOC} > \mathrm{SOC}^*$;
     - 2.1.2) $P_{\mathrm{load,PV}} < P_{\mathrm{FC,max}} + P_{\mathrm{batt,max}}$ and $\mathrm{SOC} < \mathrm{SOC}^*$;
     - 2.1.3) $P_{\mathrm{load,PV}} > P_{\mathrm{FC,max}} + P_{\mathrm{batt,max}}$;
     - 2.1.4) Intentional FC shutdown.
   - 2.2) FC not operating.
     - 2.2.1) $P_{\mathrm{load,PV}} < P_{\mathrm{batt,max}}$ and $\mathrm{SOC} > \mathrm{SOC}_{\min}$;
     - 2.2.2) $P_{\mathrm{load,PV}} < P_{\mathrm{batt,max}}$ and $\mathrm{SOC} < \mathrm{SOC}_{\min}$;
     - 2.2.3) $P_{\mathrm{load,PV}} > P_{\mathrm{batt,max}}$;
     - 2.2.4) Intentional FC startup.

$\mathrm{SOC}_{\max}$ and $\mathrm{SOC}_{\min}$ are maximum and minimum allowed SOC levels,[2] SOC^* is a predetermined average SOC that allows us to minimize the number of FC startup and shutdown operations, $P_{\mathrm{load,PV}}$ is the difference between load power consumption and PV production, $P_{\mathrm{FC,max}}$ is the upper limit of the FC power output, and $P_{\mathrm{batt,max}}$ is the upper limit of the battery converter power output. Table I summarizes the actions of the automatic scheduling system for each operation mode.

The main distinction among the operation modes is driven by the availability of the external network and, as illustrated in Table I, a large part of the automatic scheduling actions requires the availability of the battery SOC as well as to control the FC power output P_{FC}. For these reasons, the SOC is continuously

[2]Parameter $\mathrm{SOC}_{\min}$ is set sufficiently larger compared to the maximum discharge depth allowed by the battery manufacturer.

TABLE I
ACTIONS OF THE AUTOMATIC SCHEDULING SYSTEM FOR EACH OF THE OPERATION MODES

Operating mode	Action
Grid connected operating mode	
1.1	Battery charging so to reach the SOC_{max} value
1.2	No action
Islanded operating mode with the FC in operation	
2.1.1	P_{FC} setting lower than $P_{load,PV}$ until SOC = SOC*
2.1.2	P_{FC} setting greater than $P_{load,PV}$ until SOC = SOC*
2.1.3	Load shedding until $P_{load,PV} = P_{FC,max} + P_{batt,max}$
2.1.4	Load shedding until $P_{load,PV} < P_{batt,max}$ and, before FC shut-down, P_{FC} setting = P_{FCmax} until SOC=SOC_{max}
Islanded operating mode with the FC not in operation	
2.2.1	No action until SOC <SOC_{min}
2.2.2	FC start-up
2.2.3	Load shedding until $P_{load,PV} < P_{batt,max}$.
2.2.4	After FC start-up, if SOC<SOC*, P_{FC} setting = P_{FCmax}

estimated by the microcontroller where a specific functionality has been developed.

When the system is connected to the external network, the battery SOC is maximized in order to increase the margin relevant to the continuity of supply in the islanded operating mode.

In the islanded operating mode, the FC output is controlled in order to track target SOC^* value. The islanded operation is allowed also in case the FC is not in operation and $\mathrm{SOC} > \mathrm{SOC}_{\min}$.

The following two subsections describe the procedure adopted to continuously estimate the battery SOC. They also illustrate the relevant control algorithm that incorporates specific protection functions to avoid the intervention of the battery inverter voltage relay.

A. Battery State-of-Charge Estimation

In general, the SOC of a battery is defined as the difference between the initial battery capacity and the provided charge, in per-unit of the charge that the battery will nominally provide with reference to constant discharge rate. Several models are proposed in the literature (e.g., [21]–[24]), which are based on the following five basic criteria: i) measurement of electrolyte specific gravity; ii) battery current time-integration; iii) battery impedance/resistance estimation; iv) measurement of the battery open circuit voltage; and v) models that take into account the electrolyte temperature, discharge, rate and other battery parameters. Additionally, an accurate estimation of the SOC needs to take into account the battery environmental conditions, with particular reference to its temperature, as well as the battery behavior at different discharge rates and its life cycle. A combination of methods (ii), (iv), and (v) is summarized by the following general equation:

$$\mathrm{SOC}(t) = \frac{C(t_0) - \alpha(I,\theta)\int_{t_0}^{t} i(t)dt}{C(I,\theta)} \tag{1}$$

where $C(I,\theta)$ is the battery capacity for a constant current discharge rate I at electrolyte temperature θ, $C(t_0)$ is the battery capacity at time t_0, $i(t)$ is the instantaneous value of the battery current (both charge/discharge), α is the efficiency coefficient associated to battery charge and discharge (as first approximation assumed equal to one).

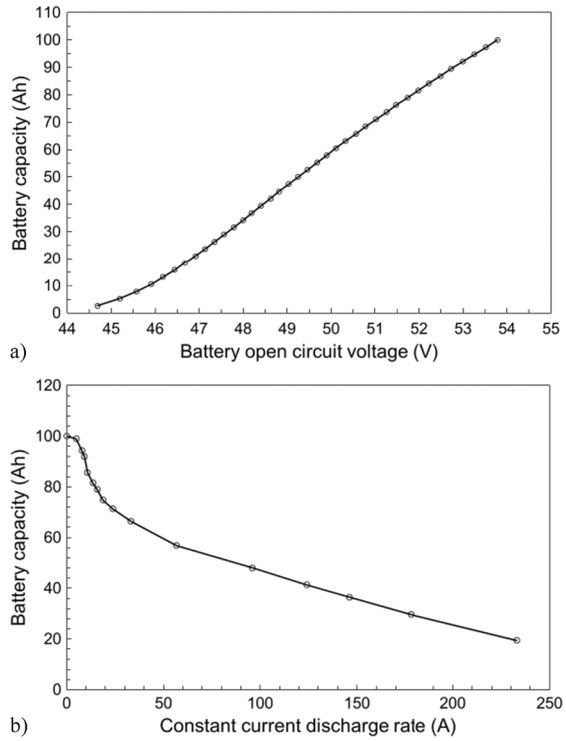

Fig. 4. (a) Relationship between the initial battery capacity (C20) and the open circuit voltage. (b) Battery capacity as a function of different constant current discharge rates of the applied 100-Ah lead-acid battery (20 °C reference temperature).

The initial battery capacity, with zero battery current condition maintained for a few hours, is based on the well-known correlation between lead-acid battery open circuit voltage and the electrolyte density [25] in the assumption that appropriate use/maintenance of the battery has been always granted. Fig. 4(a) shows such a correlation for the 100-Ah–48-V lead-acid battery storage system used in the experimental microgrid (20 °C reference temperature). It is worth noting that the initial battery capacity (C20) provided by Fig. 4(a) takes into account the battery temperature by means of the same linear approximation described below and adopted to correct the battery state-of-charge during the battery charge/discharge cycles.

The PMS includes a suitable procedure in order to apply (1) for the case of nonconstant charge/discharge rates. In particular, we assume to know the array of values $C(I^*) = (C(I_0^*), \ldots, C(I_k^*), \ldots, C(I_n^*))$ that defines the battery capacities at various constant discharge rates I_k^* at a fixed temperature θ^*. These data are typically provided by the battery manufacturer as shown in Fig. 4(b) for the adopted 100-Ah lead-acid. Alternatively, they can be easily determined by means of specific tests. The PMS calculates the average charge/discharge battery current $\tilde{I}_{T,f_s}$ within a specific time window T by averaging the measured battery current I_{batt} sampled at frequency f_s (in our case, $f_s = 5$ Hz, and $T = 2$ s). Let us assume that the SOC value has been already estimated at time $t - \Delta t$ and let us consider that $\tilde{I}_{T,f_s} \in [I_k^*, I_{k+1}^*]$ (where

I_k^* indicates various constant discharge rates at a fixed temperature θ^* used to define the array $C(I^*)$) is calculated within $[t-\Delta t, t]$ ($\Delta t = 1/f_s$, therefore, in our case, $\Delta t = 200$ ms).

Then, (1) can be written as

$$\mathrm{SOC}(t) = \frac{C(t-\Delta t) - \left(\tilde{I}_{T,f_s}(t-\Delta t) + \tilde{I}_{T,f_s}(t)\right)\frac{\Delta t}{2}}{C(\tilde{I}_{T,f_s},\theta)} \quad (2)$$

where

$$C(\tilde{I}_{T,f_s},\theta) = \frac{C\left(I_k^*\right) + C\left(I_{k+1}^*\right)}{2}. \quad (3)$$

The averaging of the charge/discharge battery current over a sufficient large time window T allows us to consider an equivalent constant discharge ratio, $\tilde{I}_{T,f_s}$, for which the application of (1) can be assumed still valid. A discontinuity in the SOC estimation could take place when the calculated average charge/discharge battery current $\tilde{I}_{T,f_s}$ switches from a discharge rate interval to a different one, i.e., when, at time t, $\tilde{I}_{T,f_s} \in [I_j^*, I_{j+1}^*]$ with subscript $j \neq k$ of (3). In order to avoid such a discontinuity in the SOC estimation, the value of battery capacity $C(t-\Delta t)$ in (2) is calculated as the product between the rated battery capacity associated to the new equivalent discharge rate $\tilde{I}_{T,f_s}$ and the SOC value estimated at $t-\Delta t$, namely

$$C(t-\Delta t) = C(\tilde{I}_{T,f_s},\theta)\mathrm{SOC}(t-\Delta t). \quad (4)$$

The rated capacity $C(\tilde{I}_{T,f_s},\theta)$ in (2) and (4) takes into account the capacity drift with the temperature adopting a linear approximation [25]

$$C(\tilde{I}_{T,f_s},\theta) = C(\tilde{I}_{T,f_s},\theta^*)\left(1+\beta(\theta-\theta^*)\right). \quad (5)$$

For the adopted lead-acid battery, coefficient β has been assumed equal to 0.006 Ah/°C (as suggested by the battery manufacturer) and the reference temperature $\theta^* = 20$ °C.

B. Experimental Validation of the SOC Estimation

The proposed algorithm for the SOC estimation has been validated by means of the experimental procedure described below.

The initial battery SOC is adjusted to be equal to 50%. After, the microgrid is operated with variable load profiles in order to simulate realistic operating conditions. The test is stopped when the estimated SOC reaches a predefined final estimated value. Different tests have been performed for different final estimated SOC values equal to 30%, 40%, 50%, and 60%. At the end of each test, the battery is disconnected from the microgrid and discharged with a constant current, corresponding to a given discharge rate, in order to determine the SOC value considered to be the true one.

Concerning the adopted procedure, it is worth noting that, in order to properly compare estimated and true SOC values, the array $C(I^*) = (C(I_0^*), \ldots, C(I_k^*), \ldots, C(I_n^*))$ must make reference to the same minimum battery discharge voltage adopted to stop the constant-current discharge test used to determine the true SOC (in our case, 1.75 V per cell, namely 42 V for the whole battery pack). Additionally, the true SOC has to be suitably corrected by taking into account the average battery temperature during its constant current discharge.

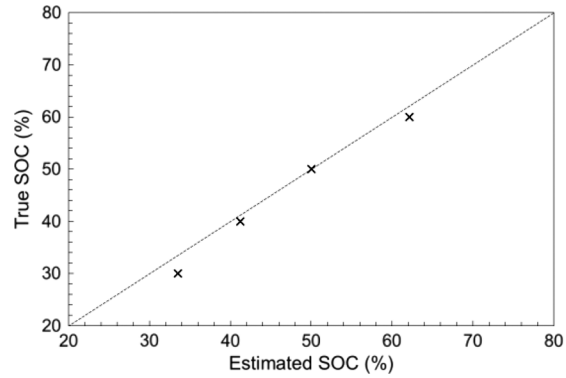

Fig. 5. Comparison between true and estimated battery SOC with reference to the different estimated SOC values.

Fig. 5 compares true and estimated battery SOC with reference to the different estimated SOC values. As it can be seen, agreement between true and estimated SOC values is good with a maximum error of 3.3% in correspondence of $\mathrm{SOC} = 30\%$.

C. Control Strategy and Limiters of the Battery Voltage

As shown in Table I, the PMS has been conceived to control the battery SOC. In particular, the FC output is controlled in order to track a target SOC value, SOC^*, which is predetermined as an average SOC level allowing us to: i) keep the storage system in a state that is able to supply energy in case of load request, or receive energy in case of positive net power produced by PV and load aggregation; and ii) minimize the number of FC startup and shutdown manoeuvres. When the SOC value is close to SOC^*, the FC output is expected to follow the load profile.

Two values, called $\mathrm{SOC}^*_{\min}$ and $\mathrm{SOC}^*_{\max}$, are chosen in order to define a relatively narrow band around SOC^* target value. The action of the control implemented into the PMS when the FC is in operation (operating modes 2.1.1 and 2.1.2 of Table I) is defined by the following four intervals associated with the battery SOC:

1) $\mathrm{SOC} \leq \mathrm{SOC}^*_{\min}$;
2) $\mathrm{SOC}^*_{\min} < \mathrm{SOC} < \mathrm{SOC}^*$;
3) $\mathrm{SOC}^* \leq \mathrm{SOC} < \mathrm{SOC}^*_{\max}$;
4) $\mathrm{SOC}^*_{\max} \leq \mathrm{SOC}$.

In correspondence of SOC intervals 2 and 3, the PMS sets the reference of the internal FC power output control, $P_{\mathrm{FC,ref}}$, in order to add or subtract an adjustment quantity proportional to the SOC deviation from the SOC^* value to the measured net power, $P_{\mathrm{load,PV}}$.

In correspondence of SOC intervals 1 and 4, the PMS sets the $P_{\mathrm{FC,ref}}$ to a value such to quickly charge or discharge the battery, respectively, in order to bring the SOC value within the band defined by $\mathrm{SOC}^*_{\min}$ and $\mathrm{SOC}^*_{\max}$ values (it is worth noting that the rate of battery charge/discharge in these operating modes depends, also, on the load request).

In all the SOC intervals, the $P_{\mathrm{FC,ref}}$ value is furthermore limited by an additional factor that takes into account the fact that

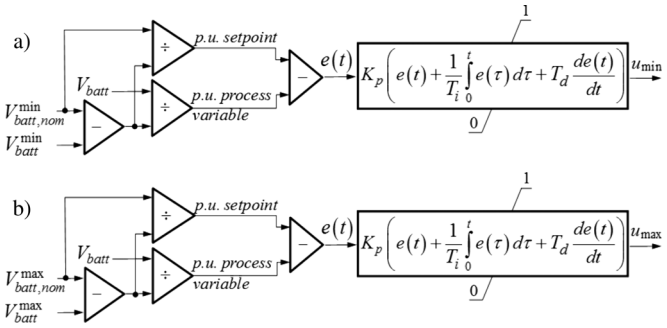

Fig. 6. (a) Battery under voltage and (b) overvoltage limiters that act to the $P_{\mathrm{FC,ref}}$ output control.

the battery power converter can operate within specific voltage limits ($V^{\min}_{\mathrm{batt}}$ and $V^{\max}_{\mathrm{batt}}$); in case of violation of these limits, an internal relay operation of the battery inverter disconnects such a component producing the microgrid blackout. As the battery voltage is varying as a function of the injected/absorbed current, such a factor, defined in the following equation by quantities $u_{\min}$ and $u_{\max}$ (both limited in the interval [0,1]), tends to limit the P_{FC} value as a function of the difference between the battery voltage V_{batt} and limits $V^{\min}_{\mathrm{batt}}$, $V^{\max}_{\mathrm{batt}}$.

For each of the four SOC intervals previously defined, the control of the $P_{\mathrm{FC,ref}}$ is, therefore, defined by the following equations:

SOC interval 1:

$$P_{\mathrm{FC,ref}} = -P_{\mathrm{load,PV}} + (P^{\max}_{\mathrm{FC}} + P_{\mathrm{load,PV}}) \cdot (1 - u_{\max}) \quad (6)$$

SOC interval 2:

$$P_{\mathrm{FC,ref}} = -P_{\mathrm{load,PV}} + (P^{\max}_{\mathrm{FC}} + P_{\mathrm{load,PV}}) \cdot \frac{\mathrm{SOC}^* - \mathrm{SOC}}{\mathrm{SOC}^* - \mathrm{SOC}^*_{\min}} \cdot (1 - u_{\max}) \quad (7)$$

SOC interval 3:

$$P_{\mathrm{FC,ref}} = -P_{\mathrm{load,PV}} + \left(P^{\min}_{\mathrm{FC}} + P_{\mathrm{load,PV}}\right) \cdot \frac{\mathrm{SOC} - \mathrm{SOC}^*}{\mathrm{SOC}^*_{\max} - \mathrm{SOC}^*} \cdot (1 - u_{\min}) \quad (8)$$

SOC interval 4:

$$P_{\mathrm{FC,ref}} = -P_{\mathrm{load,PV}} + \left(P^{\min}_{\mathrm{FC}} + P_{\mathrm{load,PV}}\right) \cdot (1 - u_{\min}) \quad (9)$$

with the constraint

$$P^{\min}_{\mathrm{FC}} \le P_{\mathrm{FC,ref}} \le P^{\max}_{\mathrm{FC}} \quad (10)$$

where $P^{\min}_{\mathrm{FC}}$ and $P^{\max}_{\mathrm{FC}}$ are the lower and the upper limits of the FC power output, equal to 500 and 4500 W, respectively.

The values of $u_{\min}$ and $u_{\max}$ are defined by means of PID controls shown in Fig. 6 that operate when the battery voltage is below, or above, two threshold values: $V^{\min}_{\mathrm{batt,nom}}$ and $V^{\max}_{\mathrm{batt,nom}}$, respectively, larger than $V^{\min}_{\mathrm{batt}}$ and lower than $V^{\max}_{\mathrm{batt}}$. The PIDs set-points, and process variables, are defined in per unit of the difference between each voltage threshold value, $V^{\min}_{\mathrm{batt,nom}}$ or $V^{\max}_{\mathrm{batt,nom}}$, and the relevant voltage limit $V^{\min}_{\mathrm{batt}}$ or $V^{\max}_{\mathrm{batt}}$.

The values of the two PIDs parameters have been assumed identical and chosen equal to: $K_p = 1$, $T_i = 30$ s, $T_d = 0.06$ s.

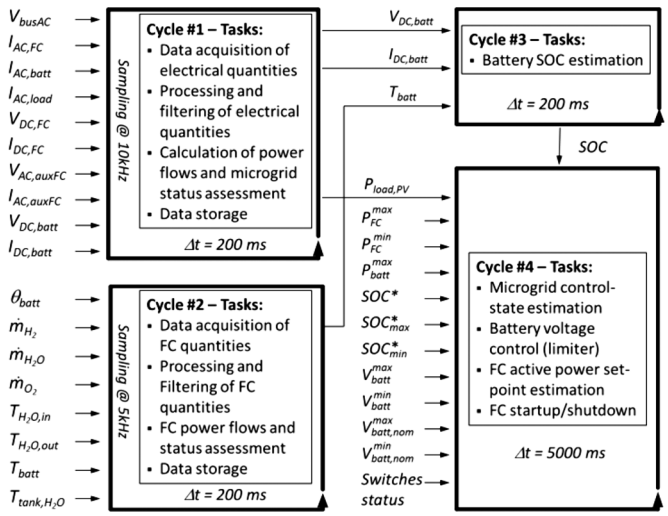

Fig. 7. Structure of the PMS implemented into the microcontroller.

D. PMS Implementation Into the Microcontroller

The FC control has been implemented into a real-time microcontroller equipped with an FPGA that allows its interface with analog/digital input/output signals. In particular, the FPGA consists of a Xilinx Virtex II 3000 device characterized by 3 M gates implementing 16-bit ADC converters, operating at a sampling frequency of 10 kHz, used to measure the system variables. The microcontroller runs four main cycles, namely: 1) data-acquisition that calculates the microgrid electrical state variables, 2) data-acquisition that determine the FC status, 3) SOC estimation; and 4) FC set point control.

Fig. 7 shows the four main cycles mentioned above. In particular, cycle #1 processes the microgrid electrical variables (sampled at 10 kHz by the ADC converters and interfaced to the microcontroller through the FPGA) in order to determine the power flows and the relevant microgrid status. The variables determined by this cycle are shared with cycle #3 (for the SOC estimation) and cycle #4 for the microgrid control-state and FC set point calculation. In particular, cycle #3 implements (1)–(5) and cycle #4 (6)–(10) as well as the PID control scheme shown in Fig. 6. Cycle #2 is responsible for determining the status of the FC in order to calculate the efficiency of the FC process.

The value of the time step loop relevant to cycle #3 (FC set point control) has been chosen equal to 5000 ms as the FC internal control is able to adjust the real FC power output with a time constant of a few seconds.

The value of time step loops relevant cycles #1, #2, and #3 has been chosen equal to 200 ms in order to adequately monitor the dynamic of power exchanges that take place into microgrid.

TABLE II
SET POINTS OF THE PV-ARRAY EMULATOR

Changing time (s)	V_{oc} (V)	I_{sc} (A)	V_{mp} (V)	I_{mp} (A)
0	0	0	0	0
10	60	6.4	51.5	5.6
40	60	5.6	51.0	4.9
130	60	7.2	52.0	6.3
210	60	8.0	52.5	7.0
900	60	4.0	50.0	3.5

TABLE III
SET POINTS OF THE LOAD EMULATOR

	Test a	Test b
Changing time (s)	P_{load} (W)	P_{load} (W)
0	0	0
10	3500	2500
110	500	5000
290	1500	3000
340	0	3000
390	2500	4500
490	3000	4000
540	500	5000
590	1200	3500
690	500	5000
940	1500	3000

IV. EXPERIMENTAL INVESTIGATION OF THE STANDALONE OPERATION

This section presents the results of some experimental tests carried out in order to verify the PMS operation with reference to the standalone case. Two conditions have been tested with reference to different SOC initial values, namely lower (Test a) and greater (Test b) than SOC^*. Both tests have been performed with the following parameters: $\text{SOC}^* = 50\%$, $\text{SOC}^*_{\text{min}} = 47.5\%$, $\text{SOC}^*_{\text{max}} = 52.5\%$, $V^{\text{min}}_{\text{batt,nom}} = 44$ V, $V^{\text{max}}_{\text{batt,nom}} = 54$ V, where $V^{\text{min}}_{\text{batt}} = 41$ V and $V^{\text{max}}_{\text{batt}} = 63$ V are the dc undervoltage relay and overvoltage relay thresholds of the battery inverter, respectively.

As mentioned, the PV generator consists of a PV-array emulator and a separated inverter that implements a maximum power point tracking algorithm. The emulator simulates the voltage–current characteristics of the solar array by means of the exponential model described in [26]. The parameters used by such a model are the following: V_{oc} (solar array cells open circuit voltage), I_{sc} (solar array cells short circuit current), V_{mp}, and I_{mp} (voltage and current of the solar array cells in correspondence of the maximum power). Table II shows the parameters used in the PV-array emulator to define the adopted production profile.

The electric load emulator consists of two separated transformers equipped with on-load tap changers (400 tap positions) that control the voltage (in the range between 0 and 230 V) applied to 9-Ω resistive and 12-mH inductive loads, respectively. The load control is realized by a hysteresis regulator that adjusts the transformer tap changer positions in order to track active and reactive power set points within a hysteresis window of ±100 W or Var.

The tests refer to two different load profiles (Test a and Test b) shown in Table III, characterized by the same duration of 1380 s. The power factor is kept constant and equal to 0.85.

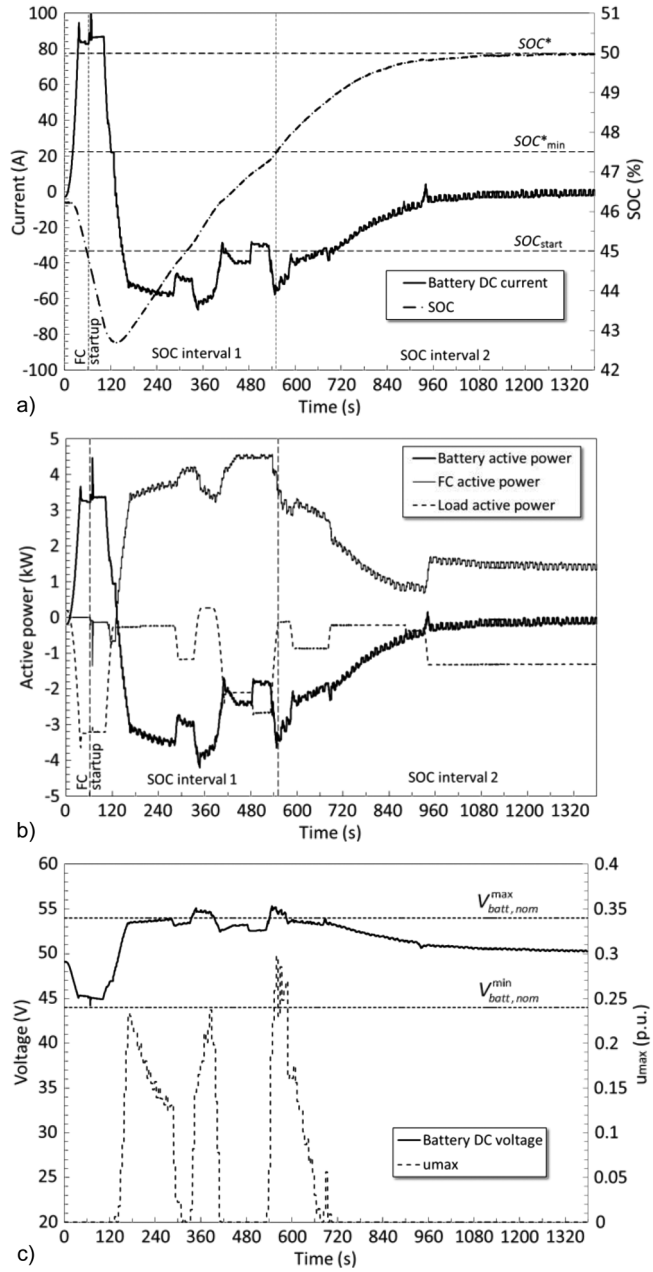

Fig. 8. Test a: (a) battery SOC and current, (b) powers (FC, battery, and net load), and (c) battery voltage and overvoltage limiter output.

A. Test a)

In what follows, we refer to the results shown in Fig. 8 where some of the measured quantities during the test are illustrated. The SOC value and the current measured at the battery dc terminals are shown in Fig. 8(a). The FC output, the power at the battery inverter ac terminals, and the profile are shown in Fig. 8(b). Fig. 8(c) shows the battery dc voltage and PID output $u_{\max}$ that limits the $P_{\text{FC,ref}}$ value using as a reference the parameter $V^{\max}_{\text{batt,nom}} = 54$ V in order to avoid the overvoltage relay intervention [as described in Fig. 6(b)].

During the performed test, the lead-acid battery temperature is different from the reference temperature $\theta^* = 20$ °C. The battery temperature increases from 22.5 °C at $t = 0$ s to about 25 °C at the end of the test.

The initial SOC value is equal to 46.2% and in these conditions the FC is not in operation. Then, the first step of the load profile of 3.5 kW and 2.2 kvar rapidly reduces the battery SOC to 45% (see Fig. 8 at 62 s), a value that has been chosen for this specific test to trigger the automatic FC startup. The FC startup lasts around 45 s. During such an interval, the FC absorbs from the battery the power needed by its auxiliaries to perform the FC startup procedure. Once the FC starts to produce power, the PMS acts to maximize the FC output in order to quickly recharge the battery (SOC interval 1), without violating the maximum dc voltage value, as set by (6). At $t = 552$ s, the battery charge exceeds the $\mathrm{SOC}^*_{\min}$ value resulting in a PMS action that aims at controlling the FC output in order to follow the profile and adjusting the battery charge to the SOC^* value [(7), corresponding to SOC interval 2].

During this test, the total energy request by the loads (taking into account also the PV production) is equal to 0.414 kWh, the FC production is 0.844 kWh, and its net electric efficiency, with reference to the hydrogen lower heating value, is equal to 37.4%. The stack production is 1.123 kWh, the auxiliaries' energy consumption (without the inverter losses) is 0.131 kWh, and the hydrogen consumption is 0.758 Nm^3. The energy accumulated in the battery is 0.358 kWh, while 0.427 kWh is the net energy absorbed by the battery storage system from the microgrid.

B. Test b)

Fig. 9 shows some of the measured quantities during the test: the SOC and the battery current profiles in Fig. 8(a), the FC output and the battery power exchange in Fig. 8(b) together with the profile, while Fig. 8(c) shows the dc battery voltage and the $u_{\max}$ PID output.

Battery SOC at the beginning of test b is equal to 52.7%, i.e., greater than $\mathrm{SOC}^*_{\max}$. The FC is operating at the minimum value $P^{\min}_{\mathrm{FC}} = 500$ W and the battery temperature varies from about 22 °C to about 25 °C.

As set by (9), corresponding to SOC interval 4, the PMS initially acts quickly to discharge the battery by reducing the P_{FC} as low as possible, taking into account also the limit of the undervoltage relay of the battery inverter. At $t = 45$ s, the battery SOC is below the $\mathrm{SOC}^*_{\max}$ threshold and then the PMS controls the FC output in order to follow the load variations with a limited shortage so to adjust the battery charge to the SOC^* value [(8), corresponding to SOC interval 3]. However, due to both the slow FC dynamic and a load value greater than $P^{\max}_{\mathrm{FC}}$, at $t = 223$ s the battery SOC becomes lower than SOC^* and afterwards the PMS adjusts the $P_{\mathrm{FC,ref}}$ to charge the battery (SOC interval 2), taking into account the $V^{\max}_{\mathrm{batt}}$ limit. As shown in Fig. 9(c), the output of the overvoltage limiter becomes greater than zero at $t = 590$ s for a short period, because of the PID derivative action.

During this test, the total energy request by the loads (taking into account also the PV production) is equal to 1.386 kWh, the FC production is 1.376 kWh, and its net electric efficiency with reference to the hydrogen lower heating value is equal to 37.6%. The stack production is 1.807 kWh, the auxiliaries' energy consumption (without the inverter losses) is 0.182 kWh, and the hydrogen consumption is 1.231 Nm^3. The energy provided by the battery is 0.108 kWh, while 0.013 kWh is the net energy provided by the battery storage system to the microgrid.

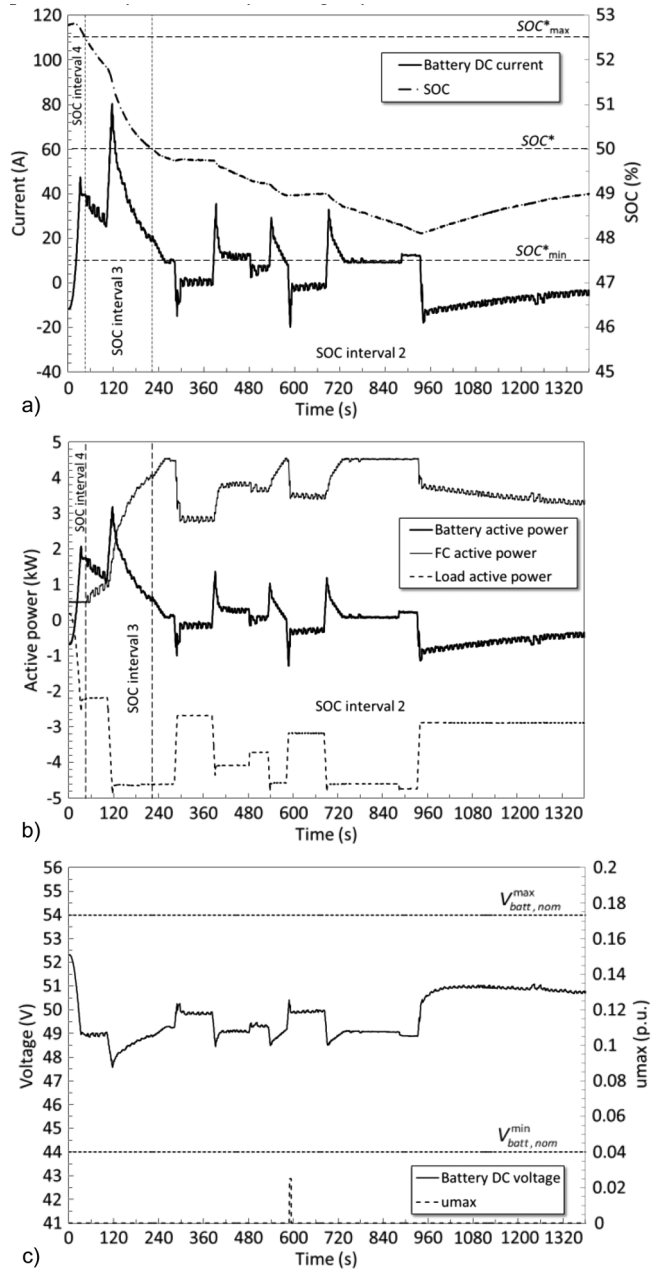

Fig. 9. Test b: (a) battery SOC and current, (b) powers (FC, battery, and net load), and (c) battery voltage and overvoltage limiter output.

V. Load Rejection Maneuver

In order to assess the capability of the PMS to control the FC to keep the battery dc voltage below the overvoltage relay threshold of the battery inverter, various tests of full load disconnections have been carried out.

As an example, Fig. 10(a) shows the measured profiles of load, battery, and FC outputs as well as $P_{\mathrm{FC,ref}}$ set by the PMS action. Fig. 10(b) shows the corresponding measured profiles of the battery voltage and current, together with overvoltage limiter output variable $u_{\max}$ [see Fig. 6(b)].

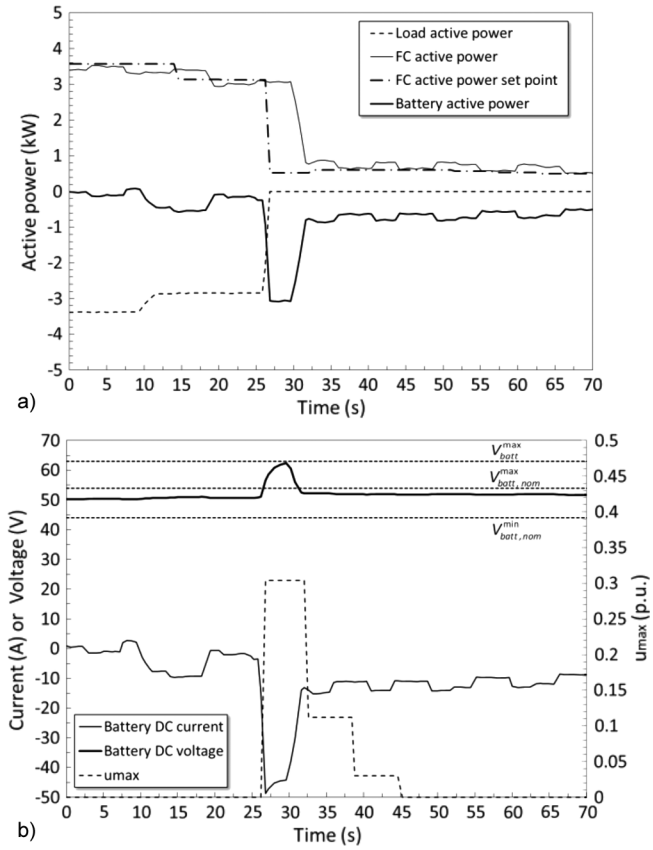

Fig. 10. Load rejection test: (a) powers ($P_{\mathrm{FC,ref}}$, FC output, battery, and net load); (b) battery voltage, current, and overvoltage limiter output $u_{\max}$.

The test starts with a 3-kW load and an SOC value equal to 49.6% corresponding to SOC interval 2. In such an initial condition, the PMS sets the $P_{\mathrm{FC,ref}}$ just above the load level. At $t = 26$ s, the main circuit breaker of the loads is opened. Fig. 10(a) shows the quick PMS response essentially due to the overvoltage limiter action shown in Fig. 10(b). The communication delay between the PMS and the FC generation curtailment is estimated to be about 3 s. The FC internal dynamic also limits the steepness of the FC output reduction. However, at $t = 32$ s, the FC output is reduced to 800 W, allowing the limitation of the voltage battery to 62.4 V and avoiding the overvoltage relay intervention and the consequent microgrid blackout. The total transient lasts for less than 6 s after which the battery voltage settles to 52 V.

VI. Conclusions

The realized PMS, described in the paper, allows the reliable standalone operation of a kW-class residential microgrid fed by a controllable FC and a PV unit. It allows following both load and PV production variations by acting on the power control of the FC. The main objective of the PMS actions is the control of the battery state-of-charge, which is estimated by using an accurate algorithm developed for this purpose: this feature represents one key aspect of the developed system compared to existing ones, as it allows limiting in an effective way the number of startup and shutdown maneuvers of the FC. The estimation of the battery state-of-charge is also a crucial parameter for the management of the energy flows in a standalone system equipped with multiple power supply and electrochemical batteries.

The action of the PID regulators has been designed/tuned in order to be adequate to avoid the intervention of the protection relays of the battery inverter also for the case of critical load rejection maneuvers.

The experimental results presented in this paper regard both the dynamic characterization of a 4.5-kW PEM FC and of a 100-Ah lead-acid battery storage system. In this respect, the obtained results appear to be an interesting complement of those recently presented in the literature by other authors (e.g., [27]–[29]) that focus mainly on the analysis of the FC characteristics.

The research framework in which the described activity has been developed is aimed also at investigating the most suitable approaches in order to exploit the heat production capability of the FC unit and at optimizing the system efficiency of the hybrid power supply: in this respect, a PMS—such as the one developed—represents a fundamental tool for accomplishing such a task.

References

[1] N. Jenkins, R. Allan, P. Crossley, D. Kirschen, and G. Strbac, *Embedded Generation*. London, U.K.: IEE, 2000.

[2] J. B. Cardell and T. Chin Yen, "Distributed energy resources in electricity markets: The price droop mechanism," in *Proc. 48th Ann. Allerton Conf.*, Monticello, IL, Sep. 29–Oct. 1 2010.

[3] F. Katiraei, M. R. Iravani, and P. W. Lehn, "Micro-grid autonomous operation during and subsequent to islanding process," *IEEE Trans. Power Del.*, vol. 20, no. 1, pp. 248–257, Jan. 2005.

[4] J. A. Peças Lopes, C. L. Moreira, and A. G. Madureira, "Defining control strategies for microgrids islanded operation," *IEEE Trans. Power Syst.*, vol. 21, no. 2, pp. 916–924, May 2006.

[5] N. Hatziargyriou, A. Asano, R. Iravani, and C. Marnay, "Microgrids," *IEEE Power Energy Mag.*, vol. 5, no. 4, pp. 78–94, Jul./Aug. 2007.

[6] B. Kroposki, R. Lasseter, T. Ise, S. Morozumi, S. Papatlianassiou, and N. Hatziargyriou, "Making microgrids work," *IEEE Power Energy Mag.*, vol. 6, no. 3, pp. 40–53, May/Jun. 2008.

[7] R. Lasseter, "Smart distribution: Coupled microgrids," *Proc. IEEE*, vol. 99, no. 6, pp. 1074–1082, Jun. 2011.

[8] N. M. Sammes and R. Boersma, "Small-scale fuel cells for residential applications," *J. Power Sources*, vol. 86, pp. 98–110, 2000.

[9] M. B. Gunes and M. W. Ellis, "Evaluation of fuel cell based combined heat and power systems for residential application," in *Proc. ASME Int. Mech. Eng. Cong. and Expo.*, New York, Nov. 11–16, 2001.

[10] M. Bagnoli and A. De Pascale, "Performance evaluation of a small size cogenerative system based on a PEM fuel cell stack," in *Proc. ASME Turbo Expo*, Reno-Tahoe, NV, Jun. 6–9, 2005, GT2005-68451.

[11] O. Erdinc and M. Uzunoglu, "Recent trends in PEM fuel cell-powered hybrid systems: Investigation of application areas, design architectures and energy management approaches," *Renew. Sustain. Energy Rev.*, vol. 14, pp. 2874–2884, 2010.

[12] P. Thounthong, S. Raël, and B. Davat, "Control algorithm of fuel cell and batteries for distributed generation system," *IEEE Trans. Energy Convers.*, vol. 23, no. 1, pp. 148–155, Mar. 2008.

[13] J. D. Maclay, J. Brouwer, and S. G. Samuelsen, "Dynamic analyses of regenerative fuel cell power for potential use in renewable residential applications," *Int. J. Hydrogen Energy*, vol. 31, pp. 994–1009, 2006.

[14] J. D. Maclay, J. Brouwer, and S. G. Samuelsen, "Dynamic modeling of hybrid energy storage systems coupled to photovoltaic generation in residential applications," *J. Power Sources*, vol. 163, pp. 916–925, 2007.

[15] B. Belvedere, M. Bianchi, A. Borghetti, A. De Pascale, M. Di Silvestro, and M. Paolone, "DSP-controlled test set-up for the performance assessment of an autonomous power unit equipped with a PEM fuel cell," in *Proc. Int. Conf. Clean Electrical Power*, Capri, Italy, May 21–23, 2007.

[16] B. Belvedere, M. Bianchi, A. Borghetti, and M. Paolone, "A microcontroller-based automatic scheduling system for residential microgrids," in *Proc. 2009 IEEE Bucharest Power Tech Conf.*, Bucharest, Romania, Jun. 28–Jul. 2 2009.

[17] S. Jain and V. Agarwal, "An integrated hybrid power supply for distributed generation applications fed by nonconventional energy sources," *IEEE Trans. Energy Convers.*, vol. 23, no. 2, pp. 622–631, Jun. 2008.
[18] W. Jiang and B. Fahimi, "Active current sharing and source management in hybrid power," *IEEE Trans. Ind. Electron.*, vol. 57, no. 2, pp. 752–761, Feb. 2010.
[19] F. Segura, J. M. Andújar, and E. Durán, "Analog current control techniques for power control in PEM fuel-cell hybrid systems: A critical review and a practical application," *IEEE Trans. Ind. Electron.*, vol. 58, no. 4, pp. 1171–1184, Apr. 2011.
[20] P. Strauss and A. Engler, "AC coupled PV hybrid systems and microgrids-state of the art and future trends," in *Proc. 3rd World Conf. Photovoltaic Energy Convers.*, Osaka, Japan, May 11–18, 2003.
[21] S. Piller, M. Perrin, and A. Jossen, "Methods for state-of-charge determination and their applications," *J. Power Sources*, vol. 96, pp. 113–120, 2001.
[22] V. Pop, H. J. Bergveld, P. H. L. Notten, and P. P. L. Regtien, "State-of-the-art of battery state-of-charge determination," *Meas. Sci. Technol.*, vol. 16, pp. R93–R110, 2005.
[23] I. Papic, "Simulation model for discharging a lead-acid battery energy storage system for load leveling," *IEEE Trans. Energy Convers.*, vol. 21, no. 2, pp. 608–615, Jun. 2006.
[24] M. Coleman, C. K. Lee, C. Zhu, and W. G. Hurley, "State-of-charge determination from EMF voltage estimation: Using impedance, terminal voltage, and current for lead-acid and lithium-ion batteries," *IEEE Trans. Ind. Electron.*, vol. 54, no. 5, pp. 2550–2557, Oct. 2007.
[25] T. B. Reddy and D. Linden, *Linden's Handbook of Batteries*. New York: McGraw-Hill, 2010.
[26] W. Lunscher, S. Britton, and M. Tanju, "A 9 kW high-performance solar array simulator," in *Proc. Eur. Space Power Conf. (ESPC)*, Graz, Austria, Aug. 23–27, 1993.
[27] M. Uzunoglu, O. C. Onar, and M. S. Alam, "Dynamic behavior of PEM FCPPs under various load conditions and voltage stability analysis for stand-alone residential applications," *J. Power Sources*, vol. 168, pp. 240–250, 2007.
[28] Y. Tang, W. Yuan, M. Pan, Z. Li, G. Chen, and Y. Li, "Experimental investigation of dynamic performance and transient responses of a kW-class PEM fuel cell stack under various load changes," *Appl. Energy*, vol. 87, pp. 1410–1417, 2010.
[29] F. Marignetti, M. Minutillo, A. Perna, and E. Jannelli, "Assessment of fuel cell performance under different air stoichiometries and fuel composition," *IEEE Trans. Ind. Electron.*, vol. 58, no. 6, pp. 2420–2426, Jun. 2011.

Bruno Belvedere was born in Bologna, Italy, in 1976. He received the M.Sc. degree in mechanical engineering, and in 2009 he received the Ph.D. degree in machine and energy systems engineering from the University of Bologna, Italy.

He worked in the University of Bologna as a Postdoc at the Department of Mechanical Engineering within the Energy System Group. He participated in various research projects and his main experimental activities relate to the integration of innovative energy sources with fuel-cell-based auxiliary power units. Since 2011, he has been working as a consultant engineer for heat management at the BMW Research and Innovation Center, Munich, Germany.

Michele Bianchi was born in Siena, Italy, in 1968. He received the M.Sc. degree with honors in mechanical engineering from the University of Bologna, Italy, and the Ph.D. degree in energy systems from the Politecnico di Bari, Italy.

Since then, he has been working with the Fluid Machines and Energy Systems group at the University of Bologna, where he was appointed Full Professor in 2011. His main research activities concern advance energy systems with particular reference to combined heat and power production, complex and integrated gas turbine cycles, and power augmentation technologies.

Dr. Bianchi is member of ASME and session organizer of IGTI.

Alberto Borghetti (M'97–SM'03) was born in Cesena, Italy, in 1967. He received the laurea degree (with honors) in electrical engineering from the University of Bologna, Italy, in 1992.

Since then, he has been working with the power system group at the University of Bologna, initially as a researcher and since 2004 as Associate Professor of Electric Power Systems. His main research interests concern power system analysis and optimization, power system restoration after blackout, electromagnetic transients due to lightning, distribution system operation, and microgrids. He is Associate Editor of IEEE TRANSACTIONS ON SMART GRID.

Carlo Alberto Nucci (M'91–SM'02–F'07) was born in Bologna, Italy, in 1956. He received the M.Sc. degree with honors in electrical engineering in 1982 from the University of Bologna.

He was a researcher with the Power Electrical Engineering Institute in 1983. He was named Associate Professor with the University of Bologna in 1992, and Full Professor and Chair of Power Systems, in 2000. He is the author or coauthor of more than 200 scientific papers published in reviewed journals or presented at international conferences. In CIGRE, he serves as chairman of the Study Committee C4 "System Technical performance." His research interests concern power systems transients and dynamics, with particular reference to lightning protection of power lines, system restoration after blackout, and smart grids.

Dr. Nucci is a Fellow of the IET. Since January 2010, he is the Editor in Chief of the *Electric Power System Research Journal*, Elsevier. He is doctor honor is causa of the University Politehnica of Bucharest.

Mario Paolone (M'07–SM'10) was born in Campobasso, Italy, in 1973. He received the M.Sc. degree (with honors) in electrical engineering and the Ph.D. degree from the University of Bologna, Italy, in 1998 and 2002, respectively.

In 2005, he was appointed Researcher in Electric Power Systems at the University of Bologna where he was with the Power Systems Laboratory until 2011. In 2010, he received Associate Professor eligibility from the Politecnico di Milano, Italy. Currently, he is Associate Professor at the Swiss Federal Institute of Technology, Lausanne, Switzerland, where he accepted the EOS Holding Chair of Distributed Electrical Systems Laboratory. He is secretary and member of several IEEE and Cigré Working Groups. He was cochairperson of the technical committee of the ninth edition of the International Conference of Power Systems Transients. His research interests are in the area of smart grids, with particular reference to real-time monitoring and operation, power system protections, power systems dynamics, and power system transients with particular reference to LEMP-interaction with electrical networks.

Antonio Peretto was born in Rovigo, Italy, in 1965. He received the M.Sc. degree (with honors) in nuclear engineering from the University of Bologna, Italy.

Since then, he has been working with the Fluid Machines and Energy Systems group at the University of Bologna, where he was appointed Associate Professor in 1998. In 2001, he became Full Professor with Bologna University and Chair of Energy Systems. His main research activities concern fossil fuel power plants, advance energy systems, with particular reference to combined heat and power production, complex and integrated gas turbine cycles, and power augmentation technologies. He is the author of 100 scientific papers published in reviewed journals or presented at international conferences. He is Chief of the Mechanical degree course at the Engineering Faculty of Bologna.

Dr. Peretto is member of ASME and session organizer of IGTI. He is also referee for European Commission of European projects on energy production systems.